Precipitation/Dissolution of Calcium Carbonate in Wellbore Cement and its Implications for the Seal Integrity of Abandoned Wells

Edward N. Matteo [1,2*], Bruno Huet [3], and George W. Scherer [4]

[1] Princeton University
Department of Chemical Engineering
Princeton, NJ 08544 USA

[2*] Current Affiliation, Corresponding Author
Sandia National Laboratories
Nuclear Waste Disposal Research and Analysis
PO Box 5800, MS-0779
Albuquerque, NM 87185 USA
Tel : +1 505 844 8923, Fax : +1 505 844 2348
enmatte@sandia.gov

[2] LafargeHolcim R&D
95 rue de Montmurier
38291 Saint-Quentin-Fallavier, France
bruno.m.huet@lafargeholcim.com

[3] Princeton University
Department of Civil & Environmental Engineering
Eng. Quad. E-319 Princeton, NJ 08544 USA
scherer@princeton.edu

ABSTRACT: Wellbore integrity of abandoned wells is of high priority for ensuring the containment of sequestered CO_2. Carbonic acid formed when injected CO_2 mixes with subsurface brines has the potential to damage well cement so as to compromise the seal integrity of the wellbore. Bench-scale experiments reported in the literature indicate that the well cement reaction rates are initially fast enough

to constitute a potential threat to wellbore integrity. However, it has also been suggested that the formation of calcium carbonate within the cement effectively arrests the acid attack by forming a passivation layer (so called “self-sealing”) that prevents further leaching of cement minerals. A broader theoretical context is presented here that delineates brine composition regimes that will instigate self-sealing in cement during carbonic acid attack.

Simulation results from a coupled geochemical reactive transport model show a dramatic drop in cement reactivity within a specific CO_2 concentration range (10 to 0.1 mM) when there is a zero calcium concentration in the brine. These simulations are complemented by bench-scale cement leaching experiments that confirm the abrupt decrease in cement reactivity in the predicted range. Analysis of the leaching experiments shows that both increases or reductions in reactivity are due to calcite precipitation. Simulations and experimental results are used to delineate four asymptotic regimes for cement reactivity depending on calcium, HCl and CO_2 brine concentrations. These regimes explain the occurrence of self-enhancing or self-sealing in a larger context, and the applications of these findings are discussed in the context of predicting wellbore integrity in abandoned wellbores exposed to carbonated brine, as well as improving interpretation of both bench-scale cement leaching experiments,.

Keywords: Acid leaching of Portland cement, carbonic acid, Class H cement, geologic CO_2 storage, wellbore integrity, calcite dissolution and precipitation

1. Introduction

Carbon sequestration has been identified as viable technological strategy for reducing and stabilizing carbon emissions worldwide [1, 2]. Ensuring that sequestered CO_2 remains in the intended subsurface storage formation is important both to prevent CO_2 from being re-released to the atmosphere through leakage, as well as to prevent environmental damage resulting from a migrating CO_2 plume that transports subsurface contaminants into ecosystems via shallow aquifers. It is widely acknowledged that abandoned wellbores represent a potential leakage pathway for migrating CO_2, allowing not only pathways for re-release at the surface, but also potentially providing access to hydrogeological units that may lie between the CO_2 storage formation and the surface. In this context, the durability of Portland wellbore cement upon exposure to carbon dioxide-saturated brine is of principal importance in determining the permanence of carbon sequestration in any subsurface formations that are intersected by abandoned wells. As thousands of abandoned wellbores may penetrate into the subsurface within the areal extent of an injected carbon dioxide plume (for example, Permian Basin in Texas, USA) [3, 4], the seal integrity of each wellbore could potentially be compromised by carbonic acid-induced damage, thus creating leakage pathways that would enable the migration of CO_2 from the storage formation. The reaction of wellbore cement with carbon dioxide-saturated brine causes decalcification of the cement matrix at rates that are well documented in the literature [5, 6]. A mechanism in which calcium carbonate forms at the leading edge of reaction has been postulated, and it has been shown that this layer plays a role in the decalcification damage mechanism. It has also been suggested that the formation of a calcium carbonate layer can, in certain instances, lead to the self-sealing of the cement wherein calcium carbonate precipitates

in the cement pores to the extent that the decalcification reaction is drastically reduced or even completely arrested.

This paper presents data from two sets of experiments that investigate the effect of the calcium carbonate layer on reactivity. The first set of experiments shows an enhanced rate of reaction that can be attributed to the carbonate layer. The second set of experiments was performed to investigate the case where the carbonate layer causes a dramatic slowdown in the rate of reaction. Geochemical modeling [7] has been used to identify key aspects of the reaction mechanism involving CO_2-bearing solution phase and Portland cement. We test a theoretical model that suggests that the carbonate layer increases the Ca^{2+} gradient and thereby enhances the attack on the cement, and which predicts that high concentrations of CO_2 (~30 mM) result in rates of attack on cement greater than those at a lower CO_2 concentration at the *same* pH. Bench top experiments at ambient conditions (22 ºC, 1 atm) performed at high and low CO_2 concentrations confirm that this phenomenon is observable at both pH 2 and pH 3. The CO_2 enhancement effect was more pronounced at the higher pH 3.

The model also predicts a steep drop in cement reactivity in the range of CO_2 concentrations between 30 mM and 0.1 mM. These simulations imply that the formation of an impermeable layer of calcium carbonate may be the cause for a dramatic drop in reactivity. Bench-top experiments in this range of CO_2 concentration were performed to confirm the occurrence of this type of so-called "pore-plugging" phenomenon. We report kinetics data, compositional profiles, and mineralogical identification that confirm that this drop in reactivity is due to formation calcium carbonate, in the form of calcite, at the leading edge of the cement reaction front, which

creates a barrier that prevents further acid ingress while sealing off unreacted cement from further reaction.

1.1 Context

Both field studies and laboratory studies have reported the formation of a calcium carbonate reaction layer in wellbore cement upon exposure to carbonic acid. Relatively fast reaction rates were reported in studies by Barlet-Gouédard [8] and Rimmelé [9], where exposure to CO_2-saturated brine resulted in a mobile calcium carbonate front. Rimmelé concludes that calcium carbonate precipitates and dissolves at or near the leading edge of the reaction front, which leads to progressive and significant reactivity of the cement matrix. Duguid and Scherer [5] also report faster reaction rates for CO_2-saturated brine in flow-through laboratory experiments (1 bar of CO2, pH 2.4 and 3.7), where the calcium carbonate layer appears between a layer of amorphous silica gel and a layer of calcium hydroxide depleted cement. Duguid et al. [10] also observes fast reaction rates and no evidence of pore clogging in a presence of a sandstone barrier (1 bar of CO2, pH 3.0, 4.0 and 5.0). These studies present evidence of a carbonate layer that is clearly part of the calcium leaching process.

Kutchko et al. [6, 11] attribute a pronounced retardation of the rate of attack to the formation of a calcium carbonate layer in quasi-batch experiments, where CO_2 was continuously recharged, while leachate accumulated in the reservoir. Similar rates and reaction patterns were found in examination of core samples taken from a wellbore exposed to a natural source of CO_2 for 30 years [12]. While the flow rate was not quantified for this field sample, the authors speculate that the reaction depths may indicate static conditions similar to the Kutchko laboratory study. A follow-up laboratory study by Wigand et al. [13] simulated a CO_2/brine leak through a fractured

wellbore, and concluded that precipitation of a layer of $CaCO_3$ – in the form of calcite, aragonite, and vaterite – led to a decrease in porosity that, in turn, blocked pores and decreased the flux of products and reactants. Again, the flow rates were slow, implying a potential pattern in the literature of static and slow-flow reaction leading to "pore plugging" by precipitation of calcium carbonate. Similarly, Luquot et al. [14] investigated cement reactivity via flow through fractured cement interfaces, and like Wigand et al. [13], reported the formation of a protective calcite layer that, once formed, prevented reaction of cement beyond the reaction front. Huerta et al. [15] also used an experimental setup that incorporates a flow through a fractured cement interface, and concluded that calcium ion concentration and pH, in addition to residence time, can result in sealing of a leaky wellbore. The work of Brunet et al. [16], based on the experimental results of Kutchko et al. [11], present a model that identifies the ratio of initial portlandite to initial porosity (vol%) as a key parameter that determines the pore-clogging potential of calcite formation.

1.2 Governing mineral reactions at equilibrium

The source of Ca^{2+} for the carbonate layer can be attributed to the dissolution of both calcium hydroxide and calcium-silicate-hydroxide (in cement chemistry notation, C-S-H):

$$Ca(OH)_2(s) \rightarrow Ca^{2+}(aq) + 2OH^-(aq) \quad (1)$$

$$\text{C-S-H (s)} \rightarrow Ca^{2+}(aq) + \text{silica gel (s)} \quad (2)$$

The formation of $CaCO_3$ can be described by the equations below:

$$Ca^{2+}(aq) + OH^-(aq) + HCO_3^-(aq) \rightarrow CaCO_3(s) + H_2O\ (aq) \quad (3)$$

$$Ca^{2+}(aq) + CO_3^{2-}(aq) \rightarrow CaCO_3(s) \quad (4)$$

where reaction (4) will dominate at pH > 10.

The precipitation of calcium carbonate can be understood in terms of the solubility product (K_{sp}), the Ion Activity Product (IAP), and the Saturation Index (SI). The equilibrium constant, *K*, for the formation of calcium carbonate (eq. 4) can be expressed as:

$$K = \frac{a_{Ca^{2+}} \cdot a_{CO_3^{2-}}}{a_{CaCO_3}} \quad (5)$$

where a_i is the activity of the species *i* and the exponent of a_i represents the stoichiometric coefficient of the species (in this case, being 1 for reactants and -1 for products). The activity of solids is unity, $a_{CaCO_3} = 1$, so we can derive the expression for K_{SP} :

$$K \cdot a_{CaCO_3} = K_{SP} = a_{Ca^{2+}} \cdot a_{CO_3^{2-}} \quad (6)$$

In a real solution [17], and not to be confused with K_{SP}, the term ($a_{Ca^{2+}} \cdot a_{CO_3^{2-}}$) is called the Ion Activity Product (IAP), and is used to define the Saturation Index (SI):

$$SI = \log\left(\frac{IAP}{K_{SP}}\right) \quad (7)$$

When SI = 0 the solid mineral is at equilibrium, when SI > 0 the solid precipitates, and when SI < 0 the solid dissolves. This expression accounts for changes in pH, ionic strength, or any other changes that may occur due to the reaction via the activity for each species. Assuming local equilibrium, K_{SP} is constant at a given temperature and pressure, so the IAP controls SI. It is clear from the IAP then, how the relative concentrations of each reactant, as well as their products, bring about equilibrium,

dissolution or precipitation. In the $CaCO_3/H_2O/CO_2$ system, in the presence of calcite, the CO_2 pressure is controlling the carbonate alkalinity, i.e. the pH and total aqueous calcium concentration.

1.3 Reaction rates

The starting point of this experimental study is a map of the key reaction mechanism regimes for cement reactivity in CO_2/H_2O (Figure 2). This diagram of pCO_2 versus pH , where pX = -log10(mX) and mX is the molality of aqueous species X, shows four distinct regions that correspond to the calculated dominant reaction mechanisms for particular concentrations of dissolved CO_2 and H+ (adjusted via HCl concentration in the following simulations). This map is based on basic principles suggested by simulation (see Figure 3) and experimental results reported in the literature. We first introduced this map since it was used to choose brine compositions in this study.

Calcium leaching occurs in any domain of the map, since the total molality of Ca^{2+} is negligible at the sample boundary. For hydrated cement paste exposed to pure water [18], HCl rich water [19] or CO_2 rich brine [7], the typical calcium concentration profile is known (see Figure 1). These profiles along with mass transfer properties of each layer define the leaching flux of calcium and therefore minerals dissolution/precipitation and front propagations. More precisely, for these three cases, the leaching flux of calcium is governed by the outer decalcified layer. Therefore the mass transfer properties of the outermost layer and the calcium concentration at the first interface (x = 1.5 mm in Figure 2) control the calcium leaching flux.

In each of the three scenarios (H_2O, CO_2 and HCl), the decalcification degree of the outermost layer does not reach the same level. In strong acid solution, this layer is

fully decalcified [20]. In CO_2-rich brine, some residual but low amount of calcium can still be observed [5], and in pure water, decalcified C-S-H remains present in this outer layer [21]. Therefore transfer properties in this outer layer differ, since the phase assemblage is not the same.

If pure water characterizes the aqueous composition at the boundary, soluble alkalies are quickly leached (no buffering capacity) and the total calcium concentration in the unreacted zone is simply governed by Portlandite solubility, i.e. $mCa^{2+} = Ca_e = 21$ mM. If HCl dominates the aqueous composition at the boundary, the calcium concentration in equilibrium with portlandite in pure water (Ca_e) is simply increased by the source of strong acid: $mCa^{2+} = Ca_e + ½\ mHCl$. Therefore on a log scale the Portlandite solubility becomes dominated by the presence of strong acid if $pH > pCa_e$ and we expect a transition between the two governing mechanisms when pH exceeds pCa_e. If CO_2 dominates the aqueous composition at the boundary, a three-layer system is observed [7] and an inversion of the gradient of calcium concentration is observed in the second layer that is rich in calcium carbonate. The calcium concentration at the interface between the outermost two layers is controlled by calcite solubility at the CO_2 partial pressure of the aqueous solution at the sample boundary. This calcium concentration is sufficient to enhance the leaching flux of calcium only if the concentration of calcium in equilibrium with calcite exceeds the concentration of calcium in equilibrium with portlandite. This condition is already achieved at 1 bar of CO_2 ($mCa^{2+} \sim 7$ mM) and at 10 bar of CO_2 ($mCa^{2+} \sim 20$ mM), which happens to be close to the dissolved CO_2 content at 1 bar ($mCO_2 \sim 30$ mM). Therefore on a log scale,

the condition $pCO_2 = pCa_e$ defines the transition from CO_2- to water-dominated calcium leaching.

When $pCO_2 > pCa_e$, i.e. when the molality of CO_2 is lower than the calcium concentration in equilibrium with portlandite (Ca_e), simulation results seem to suggest that a pore clogging mechanism could occur (see Figure 3). Indeed, a discontinuity is observed on the map of cement reactivity as a function of pCO2: the initial cement reactivity drops by almost two orders of magnitude before the fronts eventually stop moving. These simulation results are obtained using the same model and same cement composition as in [7]; only the dissolved CO_2 molality is adjusted in the range [1.e-5, 1.0] M and the pH maintained constant at 3.7 by adding either HCl or $NaHCO_3$ in the system. These results suggest that for some intermediate CO_2 concentrations, a pore-clogging mechanism may occur in the absence of aqueous calcium at the boundary. The exact boundary of the clogging domain is not yet understood and is represented by a dashed line on the reactivity map (Figure 2).

When both HCl and CO_2 molalities are larger than the calcium molality governed by portlandite solubility (CaO/H_2O pure system), we expect a transition between the two mechanisms (CO_2 and H_2O) if pH ~pCO_2. Thus, the concentration of calcium in equilibrium with portlandite, Ca_e, along with brine composition is a key indicator of the governing mechanism and the transition between them.

The aim of this work is to collect experimental evidence that will contribute in refining, confirming or denying the above proposed mechanisms. A second companion paper using reactive transport modeling [22] further expands the analysis of governing

processes by investigating not only the contributions of water composition, but also the initial cement composition and the mass transfer properties of each layer.

2. Methods

Cement samples were prepared from Class H Portland cement at a water/cement ratio ~ 0.4 and cured a minimum of 6 months prior to acid exposure. The details of sample preparation and the flow-through imaging apparatus are described elsewhere, as are the details of the imaging setup used to track and measure the ingress of the reaction front at 30X magnification [23].

2.1 Aqueous compositions

Experimental conditions for individual experiments were chosen on the basis of the findings of simulations that modeled enhanced cement leaching by carbonic acid under specific concentration of carbon dioxide. The range of parameters tested the role of pH and dissolved CO_2 concentration on the carbonic acid reactivity of Class H cement, as described in the background (Section 1.2). Specific aqueous compositions are chosen in the CO_2, H_2O and Clogging domain (see Table 1 and Figure 2). Aqueous solutions are prepared with standard chemicals and gas. Solution F is not controlled by a gas buffer and specific care was taken (see section 2.2 for specific details).

2.2 Protocol for Achieving Sub-saturated levels of CO_2 (< 30mM)

To achieve dissolved concentrations of CO_2 below that of an aqueous solution in equilibrium with 1 bar CO_2 (~30 mM), a specialized experimental protocol was implemented, requiring: A) minimizing contact between the acid solution and the atmosphere, to prevent equilibration between the aqueous solution and CO_2 in the atmosphere that would result in an decrease in CO_2 content below the intended concentration; and B) utilizing the following chemical reaction between hydrochloric acid (HCl) and sodium bicarbonate ($NaHCO_3$) to control the concentration of CO_2 dissolved in the aqueous acid solution:

$$NaHCO_3(s) + HCl\,(aq) = NaCl\,(aq) + H_2O(aq) + CO_2\,(aq) \qquad (8)$$

For example, if 10 mM of HCl and 10 mM of $NaHCO_3$ are mixed, the resulting aqueous solution, if kept isolated from the open atmosphere, will have 10 mM concentration of dissolved CO_2.

Preliminary tests of this chemistry were run in a 1L Erlenmeyer flask, the top of which was covered with parafilm as soon as the reactants were mixed in solution. The pH was monitored by a pH meter and proved to be steady for over a month and no precipitate formation was observed. To perform the cement leaching experiments, larger volumes of this solution were required. Five-gallon polyvinyl chloride (PVC) bags were used as vessels to hold the aqueous mixture and ensure that it remained isolated from ambient CO_2. The PVC bags functioned in a manner similar to that of a medical intravenous bladder, with the aqueous solution actively pumped out of the bag by a peristaltic pump; the absence of head-space prevents evaporation of CO_2 from the solution.

2.3 SEM-EDS/ESEM Procedures for Chemical Analysis

Energy dispersive X-ray spectroscopy (EDS) was used to analyze the cross-sectional chemical composition of dried samples. Given the sensitivity of EDS to height differences on the surface of the sample, leveling and polishing of the sample is standard practice. Generally this is done after encasing or embedding the sample in epoxy, which is necessary when trying to polish a fragile, porous sample like the acid-leached cement layers in these samples.

Drying-induced effects were qualitatively assessed by comparing the volume and pore features of an undried sample imaged using Environmental Scanning Electron Microscopy (ESEM) with an SEM image of a dried sample. Additionally, a comparison was made between a dried sample and an epoxy-embedded, dried sample to check for compositional, mineralogical, or microstructural artifacts created during the polishing process.

The first step in preparing dried samples is to perform a solvent exchange to isopropanol (IPA) for a minimum of 1 week, with the IPA solution replenished at regular intervals. Due to the fact that IPA is relatively chemically unreactive with Portland cement, it produces less disruption of the pore network (relative to aqueous solution) upon drying [24]. After solvent exchange, the samples were dried under nitrogen for a minimum of a week. The dried samples were embedded in Buehler EPO-THIN epoxy and cured under a vacuum. The epoxy-encased samples were trimmed, leveled, and wet polished to 1200 grit with paper and then to 0.1 μm with colloidal spheres on a lapping wheel.

Given the heterogeneous nature of cement paste, care was taken when selecting the method of surface averaging used for compositional analysis via SEM/ESEM. Compositional profiles were obtained by performing area scans with dimensions of 100 μm X 100 μm. The composition measured via this method was compared with point-by-point grids, and the profiles were found to be nearly identical (see Appendix 1). Therefore, we conclude that a 100 μm cube is a reasonable Representative Volume Element (RVE) for cement paste.

Tests were performed to ascertain the effect of grid resolution on elemental composition, i.e. the number of EDS spots per μm^2. It was found that, in general, the leached layers closest the cement/acid interface (and therefore the most heavily leached) were less sensitive to increases in the grid resolution than the relatively un-leached regions. This is due to the fact that these regions are more homogeneous, and therefore have a smaller RVE than the unreacted cement. Ultimately, the area scan feature of the INCA EDS software, in which the user selects an area of interest over which the composition is averaged, proved to be as accurate as the procedure of creating a grid of points over the same area and computing the composition by averaging each grid point within the grid area. The area scan method was used to create compositional profiles of areas that were approximately 100 x 100 μm.

2.4 Electron Back-Scattered Diffraction for Mineralogy

Mineralogical phase identification can be obtained from the polished samples using Electron Back-Scattered Diffraction (EBSD). This involves using a detector in a scanning electron microscope that is specifically placed to receive back-scattered electrons from a sample titled 70º relative to the incident electron beam.

3. Results

3.1 Kinetics Results

The kinetics results relevant to this study are summarized in Figure 4 and Figure 5. Figure 4 shows data for 4 experiments that were performed at two distinct concentrations of CO_2: 0.01 mM (in equilibrium with atmospheric CO_2) and 30 mM (1 bar CO_2) for both pH 2 and pH 3 flow-through experiments. The plot clearly shows that, for both the pH 2 and the pH 3 experiments, the increased CO_2 concentration results in a faster reaction rate, and the difference is more pronounced at the higher pH 3.

Figure 5 shows the results of three experiments, all performed at pH 5.6 with a constant replenishment of acid of 75 mL/h, differing in CO_2 concentration. While all three experiments were performed under flow-through conditions, two of the experiments – at 30 mM CO_2 with SI(Calcite) = -1.0 and at 10 mM CO_2 – were designed specifically to promote pore plugging. Both clearly deviate from linear square root of time kinetics, potentially implying formation of a pore-plugging carbonate layer. For the latter experiments, the deviation is observed as soon as 1 day of exposure and reactivity completely stops between 2 and 4 days. For the former experiments, the deviation is observed after a characteristic time of ~ 15 d., the cement reactivity has not yet completely stop after 45 days of exposure, with a rate of ~1.0e-2 $mm/h^{1/2}$ which 6 times lower than the initial rate.

3.2 Compositional Profiles

Calcium-to-silica (Ca/Si) ratios were acquired via energy dispersive x-ray spectroscopy (EDS) for the samples whose corrosion rates are presented in Figure 4 and

Figure 5. Figure 6 shows a plot of the Ca/Si ratio versus normalized reaction depth for the experiments that compare high and low CO_2 concentration. The Ca/Si ratio is quite low through the reaction zone for all of the experiments except for the pH 3, 0.01 mM case. In the cases where the Ca/Si ratio is low in the reaction zone (from a normalized depth x = 0 to x = 1), it then jumps abruptly for x > 1, which represents the leading edge of the reaction zone. The depth at which the Ca/Si ratio jumps to values in the range of 1.5 - 2 represents the boundary of the calcium hydroxide depleted region. The Ca/Si ratio of unreacted C-S-H is typically ~1.7 [25].

Figure 7 shows a plot of Ca/Si ratio versus normalized depth for the pore-plugging experiments. There are large spikes in the Ca/Si ratio for both the 30 mM CO_2 and 10 mM CO_2 concentrations. The pH 5.6, 30 mM CO_2 case shows a Ca/Si ratio above 2.5 throughout the reaction zone that spikes up to ~5 at the leading edge of the reaction front. The pH 5.6, 10 mM CO_2 case shows two spikes in the Ca/Si ratio – the first spike of ~4 appears to be at the surface of the reaction zone (at the interface of the acid reservoir and cement solid phase), while the second peak, Ca/Si ratio > 6, appears at the leading edge of the reaction front.

4. Discussion

The differences in reaction rates presented in Figure 3 can be explained by the differences in reaction mechanism between the carbonic acid attack and the HCl attack. The differentiating characteristic between the two is the formation of a carbonate layer in the case of carbonic acid attack. This layer of $CaCO_3$ precipitates at the leading edge of the reaction front (between the silica gel of the reacted zone and the calcium hydroxide-leached cement) and dissolves on the edge adjacent to the silica gel. The

carbonate layer serves to enhance the rate of reaction of cement by creating a steeper Ca^{2+} gradient than would otherwise exist in the absence of the $CaCO_3$ layer.

The calcium carbonate reaction zone shown in Figure 8 has been observed in a number of acid/cement experiments [5, 6, 8, 9, 13, 14, 23], as well as in the data plotted in Figure 4 and Figure 5, for cement reactivity in contact with brine equilibrated with 1 bar CO_2. Since the solubility of calcium carbonate decreases with increasing pH or decreasing CO2 concentration, it is not surprising that the thickness of the calcium carbonate layer (for the same depth of reaction) increases with pH, as shown in Figure 8. The time-lapse movies, from which the images in Figure 8 were taken, also show that this calcium carbonate moves with the leading edge of the reaction front and becomes thicker over the course of the experiment, as shown in Figure 9 and as predicted by Huet et al. [7]. This mobility suggests that, in this instance, the carbonate layer is permeable and contributes to continuous reactivity. From Figure 9, it can also be seen that the thickness oscillates over time, suggesting that the carbonate layer dissolves and re-precipitates as the leading edge of the reaction front advances.

It is also observed that the calcium carbonate layer "flickers", i.e. contracts and expands, as it progresses with the reaction front, and at times, appears to move laterally. For example, the carbonate layer in Figure 9 appears thicker after 4 days of exposure than after 6 days, and it is thicker after 21 days than after 23 days. This behavior rules out the possibility that the layer's progressive thickening is merely the result of accumulation, but rather indicates a dissolution-precipitation mechanism. The fact that overall, and despite the flickering, the carbonate layer grows progressively thicker also implies that the changes in the relative concentrations of Ca^{2+} and total carbonate in

solution play an important role in the dynamics of the calcium carbonate layer. This phenomenon was previously documented and discussed in the literature [26, 27].

The choice of brine composition for the pore-plugging experiments (pH=5.6, 30 mM CO_2 and 10 mM CO_2) aims to 1) approach the singularity observed in Figure 3 from low CO_2 concentration (pCO2 > pCa_e, "Clogging" domain of Figure 2) and 2) reduce the leaching of calcium by increasing the calcium concentration at controlled saturation index of calcite. Both experiments depart sharply from square root of time kinetics over different time scales (), despite the fact that both employ a relatively high flow rate of acid replenishment. The kinetics imply that this change in relative concentrations, perhaps in combination with the higher pH of 5.6, bring about a precipitation of a pore-plugging calcium carbonate layer. The Ca/Si profiles of the pH 5.6 pore-plugging experiments indicate enrichment of solid calcium carbonate at the reaction front. Figure 10 shows the results from an EBSD analysis of the mineralogy in the region where the spike occurs. The pattern in Figure 10 is a very strong match for calcite and is evidence that the solid phase enrichment of calcium, indicated in the Ca/Si profile, is due to precipitation of calcium carbonate in the form of calcite.

A model proposed by Schwotzer et al. suggests that the source of Ca^{2+} is critical to determining whether the carbonate layer formed is impermeable and protective, or permeable and a contributor to reactivity of cement [28]. According to that model, if Ca^{2+} is supplied by the cement pore solution, continuous reaction will occur. If, on the other hand, the Ca^{2+} is supplied in the acid reservoir, for example, Ca^{2+}-enriched tap water, the calcium carbonate layer will be pore-plugging and protective. The results shown in Figure 5 contradict this aspect of the theory, however, since one of our pore-

plugging experiments does indeed contain Ca^{2+} in the brine reservoir, while the other does not. In fact an impermeable calcium carbonate layer forms , only after 1 day, in the sample immersed in 10 mM CO_2 concentration containing no Ca^{2+}, whereas the carbonate layer formed in the sample immersed in the 30 mM CO_2 concentration that contains calcium bicarbonate (SI(calcite)=-1.0), is still not fully impermeable after 45 days even though it does significantly reduces the reaction rate.

Figure 6 and Figure 7 report the average Ca/Si ratio with respect to normalized depth. Further inspection of microstructural features of the gel layer can also provide insight into the mechanism that leads to pore plugging. The gel regions of the two pore–plugging experiments at 10 mM CO_2 and 30 mM CO_2 (both pH 5.6) reveal different microstructural features, as shown in the SEM images in Figure 11. The sample exposed to 10 mM CO_2 shows large Ca-rich regions ranging from 10-30 μm, while the sample exposed to 30 mM CO_2 has 1-5 μm Ca-rich regions throughout the gel. The latter very much resemble features of the "protective-type" of $CaCO_3$ layer documented by Schwotzer [28]. The features in the 10 mM CO_2 sample (in Figure 11) resemble those in a non-pore-plugging sample (see Appendix 1, Figure 12), though the Ca-rich features seem more prevalent in the pore-plugging sample. This is confirmed by an average Ca/Si ratio of ~3 in the pH 5.6, 10 mM CO_2 sample versus Ca/Si ratio ~0.3 in the pH 3.7, 30 mM CO_2 sample from Figure 12. Additionally, Figure 7 shows that there are 2 peaks in the Ca/Si ratio for the 10 mM CO_2 case, while the Ca/Si ratio is constant (Ca/Si~ 2.6) through the reaction zone for the pH 5.6, 30 mM CO_2 case. The two peaks imply that there are potentially two $CaCO_3$ layers in the 10 mM CO_2 case, which, in turn, may suggest that a different mechanism is at work in each case.

While we can attribute the pore-plugging precipitation largely to the relative fluxes of Ca^{2+} and bicarbonate, the acid reservoir conditions, especially pH, also play an important role due to their effect on the solubility of $CaCO_3$. Therefore, while the relative fluxes of Ca^{2+} and carbonate are among the main driving forces for precipitation, variables with the potential to affect K_{sp}, IAP, or saturation index will also play a part in the formation of a pore-plugging carbonate layer.

The implications of these results are important not only for predicting wellbore integrity, but also for interpreting bench-top experimental results, simulations, and studies of cement cores from field samples. For example, the theoretical construct presented in this paper can be employed to predict areas along the vertical stretch of a wellbore cement sheath where pore plugging may or may not occur. Using the solubility data for CO_2 in brine of varying salinity available in the literature [29] (see Supplemental Material 2), it can be shown that pore plugging is much more likely to occur at shallower depths (< 500 m), where the concentrations of CO_2 dissolved in brine will be in the range necessary for the pore-plugging regime. Alternatively, the concentrations of dissolved CO_2 could be used in conjunction with data for calcium ion concentration in the brine of interest, to predict whether pore plugging will occur. Ultimately, knowing whether or not pore plugging occurs is important for understanding and predicting the chemo-mechanical damage in wellbore cement. In turn, understanding the extent of this damage will allow for more accurate predictions for wellbore seal integrity.

5. Conclusions

The presence of CO_2 enhances the corrosion rate of cement and the effect is more pronounced at higher pH. This effect of CO_2 concentration on the reaction rate can be explained by the enhanced Ca^{2+} gradient that results from carbonate formation in the solid phase. This carbonate layer forms by a non-plugging (permeable) dissolution-precipitation mechanism, which allows it to move with the leading edge of the reaction front. The carbonate layer is also found to have a greater overall thickness with increasing pH.

Pore plugging, in which an impermeable carbonate layer forms, is explored by bench top experiments specifically designed to test the predictions of simulations. It is found that neither pH, CO_2 concentration, nor Ca^{2+} concentration alone can lead to pore plugging. The results indicate that "flux-matching" where the relative concentration of calcium and carbonate in solution are approximately equal, results in formation of a $CaCO_3$ film that slows reaction, such that the kinetics deviate from square root of time kinetics. The Ca-rich regions of the microstructure in the reaction zone of the two pore-plugging experiments differ, which may imply that different precipitation pathways led to the formation of the impermeable carbonate layers in each case.

The implications of this work in determining seal integrity of abandoned wellbores lie in allowing for the effects of the vertical heterogeneity of the wellbore to be taken into account. Specifically, local variations in brine concentration, cement composition, temperature and pressure can influence whether or not pore plugging occurs.

6. References

[1] IPCC Fourth Assessment Report (AR4) Working Group III Report – Mitigation of Climate Change, 2007.

[2] Pacala, S. and R. Socolow. Stabilization Wedges: Solving the Climate Problem for the Next 50 years with Current Technology. Science, Vol 304, 5686, 968-972, 2004.

[3] Bachu, S., CO_2 storage in geological media: Roles, means, status and barriers to deployment. Progress in Energy and Combsution Science 34, 254-273, 2008.

[4] Gasda, S., M. Celia, and S. Bachu. Spatial characterization of the location of potentially leaky wells penetrating a deep saline aquifer in a mature sedimentary basin. Environmental Geology. Vol. 46, N. 6-7, 707-720, 2004.

[5] Duguid, A. J. and G. W. Scherer, 2010. Degradation of oilwell cement due to exposure to carbonated brine. Int. J. Greenhouse Gas Control, 4, 546-560.

[6] Kutchko, B. G., B. R. Strazisar, G. V. Lowry, D. A. Dzombak, and N. Thaulow, 2007. Degradation of Well Cement by CO_2 under Geologic Sequestration Conditions. Env. Sci. Tech. 41, 4787-4792.

[7] Huet, B., J. H. Prevost, and G. W. Scherer. Quantitative reactive transport modeling of Portland cement in CO_2-saturated water. Int. J. Greenhouse Gas Control 4, 561-574, 2010.

[8] Barlet-Gouédard, V., G. Rimmelé, B. Goffé, and O. Porcherie, 2007. Well Technologies for CO_2 Geological Storage: CO_2-Resistant Cement. Oil and Gas Science and Technology, 62, 324-334.

[9] Rimmelé, G.,V. Barlet-Gouédard, O. Porcherie, B. Goffé, and F. Brunet, 2008. Heterogeneous porosity distribution in Portland cement exposed to CO_2-rich fluids. Cement Concr. Res., 38, 1038-1048.

[10] Duguid,A., Radonjic, M., Scherer, G.W., 2011. Degradation of cement at the reservoir/cement interface from exposure to carbonated brine, Int. J. Greenhouse Gas Control, 5, 1423-1428.

[11] Kutchko, B. G., B. R. Strazisar, G. V. Lowry, D. A. Dzombak, and N. Thaulow, 2008. Rate of CO_2 Attack on Hydrated Class H Well Cement under Geologic Sequestration Conditions. Env. Sci. Tech., 42, 6237-6242.

[12] Carey, J. W., M. Wigan, S. J. Chipera, G. WoldeGabriel, R. Pawar, P. C. Lichtner, S. C. Wehner, M. A. Rainers, and G. D. Guthrie Jr., 2007. Analysis and performance of

oil well cement with 30 years of CO_2 exposure from the SACROC Unit, West Texas, USA. Int. J. Greenhouse Gas Control, 1, 75-85.

[13] Wigand, M., J. P. Kaszuba, J. W. Carey, and W. K. Hollis, 2009. Geochemical effects of CO_2 sequestration at the cement/caprock interface. Chemical Geology, 265, 122-133.

[14] Luquot, L., H. Abdoulghafour, and P. Gouze. Hydro-dynamically controlled alteration of fractured Portland cements flowed by CO2-rich brine. International Journal of Greenhouse Gas Control, 16(0):167–179, 2013.

[15] Huerta, N. H., M. A. Hesse, S. L. Bryant, B. R. Strasizar, and C. Lopano, 2016. Reactive transport of CO_2-saturated water in a cement fracture: Application to wellbore leakage during geologic CO_2 storage. International Journal of Greenhouse Gas Control, 44, 276-289.

[16] J.-P. L. Brunet, L. Li, Z. T. Karpyn, B. G. Kutchko, B. Strazisar, and G. Bromhal. Dynamic Evolution of Cement Composition and Transport Properties under Conditions Relevant to Geological Carbon Sequestration. Energy & Fuels, 27(8):4208–4220, 2013.

[17] Zhu, C. and G. Anderson. Environmental Applications of Geochemical Modeling, 2002. Cambridge University Press, Cambridge.

[18] Adenot F., A. Aspart. Modélisation de l'influence du débit de renouvellement de la solution agressive sur la cinétique de dégradation d'une pâte de ciment, in: Sci. Des Mater. Procedes Des Betons Premieres Rencontres Int., 1998: pp. 141–149.

[19] Alexander, M, A. Bertron, N. De Belie, Performance of Cement-Based Materials in Aggressive Aqueous Environments, RILEM State-of-the-Art Reports, Vol. 10, 464 P., 2013.

[20] Gutberlet T., H. Hilbig, R.E. Beddoe, Acid attack on hydrated cement - Effect of mineral acids on the degradation process, Cement and Concrete Research 74 (2015) 35-43.

[21] Matte, V., M. Moranville, F. Adenot, C. Richet and J.M. Torrenti, Simulated microstructure and transport properties of ultra-high performance cement-based materials, Cement and Concrete Research 30 (2000) 1947–1954.

[22] Georget, F., Prevost, J.-H., Huet, B., Reactive transport modelling of cement paste leaching in brines, this volume.

in brines

[23] Matteo, E. N. and G. W. Scherer, 2012. Experimental Study of the Diffusion-Controlled Acid Degradation of Class H Portland Cement. Int. J. Greenhouse Gas Control, 7, 181–191.

[24] Zhang, J. and G.W. Scherer, 2011. Comparison of methods for arresting hydration of cement. Cement Concr. Res., 41, 1024–1036.

[25] Thomas, J. J., J. J. Chen, A. J. Allen, and H. M. Jennings, 2004. Effects of decalcification on the microstructure and surface area of cement and tricaclium silicate pastes. Cement Concr. Res., 34, 2297-2307.

[26] Kirov, G. K., I. Vesselinov, and Z. Cherneva, 1972. Conditions of Formation of Calcite Crystals of Tabular and Acute Rhombohedral Habits. Kristall und Technik, 7, 497-509.

[27] Ruiz-Agudo, E., C. V. Putnis, C. Rodriguez-Navarro, and A. Putnis, 2011. Effect of pH on calcite growth at constant $a_{Ca(2+)} / a_{CO3(2-)}$ ratio and supersaturation. .Geochimica et Cosmochimica Acta, 75, 284-296.

[28] Schwotzer, M., T. Scherer, and A. Gerdes, 2010. Protective or damage promoting effect of calcium carbonate layers on the surface of cement based materials in aqueous environments. Cement Concr. Res., 40, 1410-1418.

[29] Duan, Z. and R. Sun, 2003. An improved model calculating CO_2 solubility in pure water and aqueous NaCl solutions from 273 to 533 K and from 0 to 2000 bar. Chemical Geology 193, 257-271.

7. **Supplemental Material 1: Comparison of polished versus unpolished samples**

Comparison is made between SEM images of samples impregnated with epoxy and another that is not impregnated with epoxy prior to polishing. The Back Scattered Electron image of the unpolished sample (not shown) indicates the presence of the Ca-rich region (bright flecks in the gel) ensuring that these Ca-rich regions are not an artifact created during the polishing process. There are clear advantages in identifying distinct phases in the polished, epoxy-embedded sample. The polished sample allows us to isolate different distinct regions in the gel, which was nearly impossible to do with the unpolished sample. *Figure 13 shows that there are two distinct regions in the gel. Figure 14 shows that the darker regions have a Ca/Si ~0.13, which implies no intact C-S-H, and most likely some sort of silica gel (or aluminosilicate gel). In *Figure 15, the compositional data for the bright spots shows that the bright flecks in the gel region are enriched in calcium. Since the samples are polished, it is possible to use EBSD to identify mineralogical phases within the gel. *Figure 16 shows a close-up of the Ca-rich (bright) spots in the gel layer of a pH 3.7, 1 bar CO_2 sample. EBSD is used to analyze the crystals in the Ca-rich region and it reveals the Kikuchi Pattern of calcite. *Figure 17 shows the region at the leading edge of the pH 5.6, 30 mM CO_2 sample. Figure 10 shows the EBSD "solution" of this region. For this calcite crystal, the fit corresponds to a *mean angular deviation* (MAD) of 0.917. In these types of data sets, MAD's <1 are considered to represent a good fit to the data. The above Kikuchi pattern was scanned for fits to crystals composed of the chemical elements detected via EDS, including portlandite. Only calcite was detected in the Ca-rich regions.

8. **Supplemental Material 2: CO_2 Concentration in Brine as a Function of Subsurface Depth**

The work of Duan and Sun [29] provides CO_2 concentrations at various temperatures, pressure, and salinities. Used with typical subsurface temperature and pressure gradients, estimates can be derived for CO_2 saturation as a function of subsurface depth. These calculations are shown in *Figure 17. This figure illustrates how CO_2 concentration varies with depth, as well as the effect of increased salinity. The "salting out" effect, where the solubility of CO_2 decreases with increasing salinity, is shown to vary by roughly a factor of two between the no-salt and 4M NaCl cases across the range of depths.

9. FIGURES and TABLES (* indicates supplemental figures)

Table 1: Composition of aqueous solutions used for leaching test.

Name	pCO_2	pH	$CaCl_2$	$NaHCO_3$	HCl	SI(Calcite)
	[-]	[-]	[mM]	[mM]	[mM]	[-]
A	5	2.0	-	0	1.3e-2	-
B	1.5	2.0	-	0	1.3e-2	-
C	5	3.0	-	0	1.3e-3	-
D	1.5	3.0	-	0	1.3e-3	-
E	5.0	5.6	-	1.0e-3	0	-
F	2.0	5.6	-	13	10	-
G	1.5	5.6	5.3	8	0	-1.

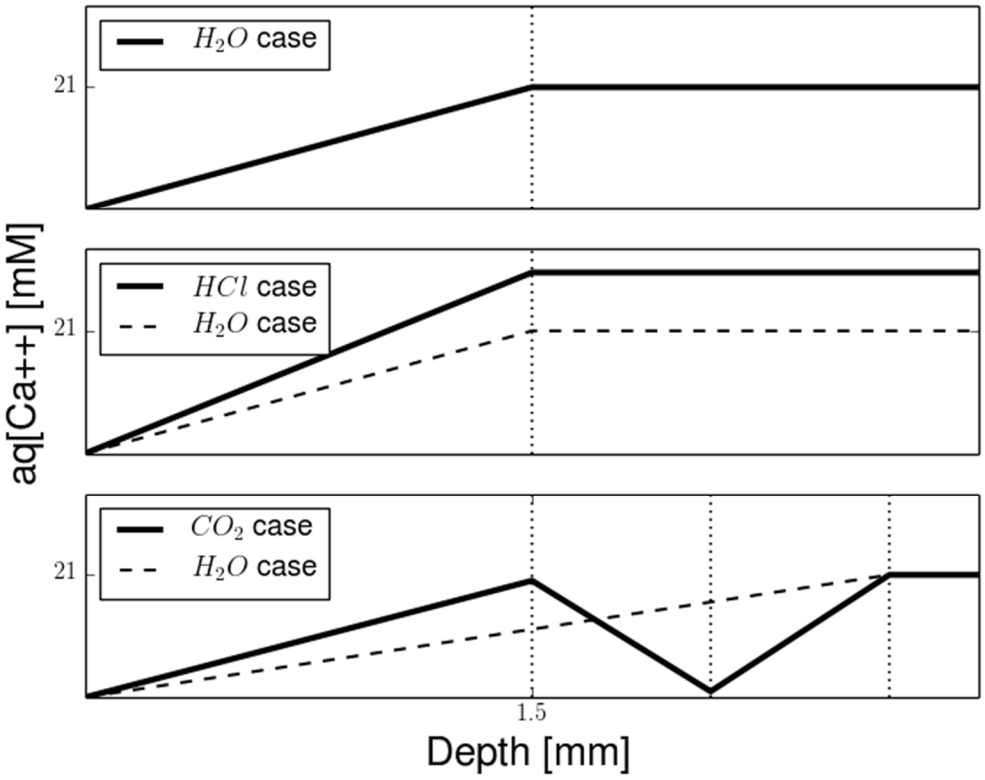

Figure 1 Typical total aqueous concentration profile during leaching of hydrated cement paste in H_2O (top), in HCl (middle) or CO_2 (bottom) dominated cases

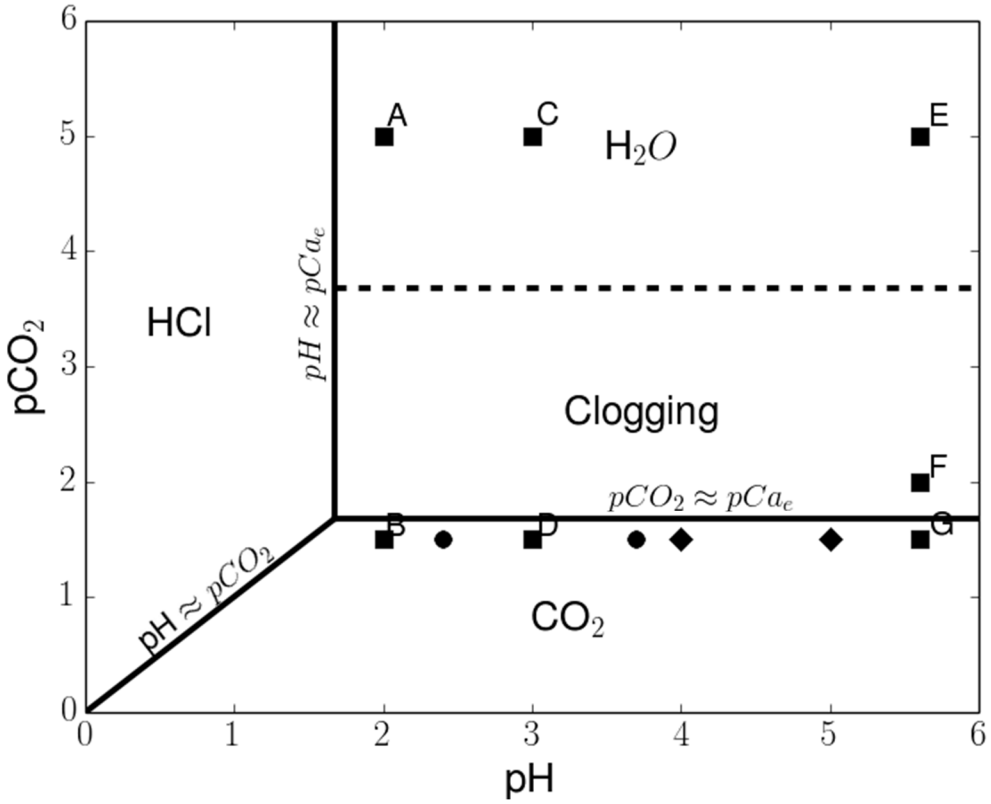

Figure 2. Illustration of the "flux matching" principle. In this figure, pCO_2 = -log[CO_2], and pCa_e = -log[Ca_e], where Ca_e is the total aqueous concentration of Ca^{2+} in equilibrium with Portlandite in pure CaO/H_2O system, i.e. ~21 mM. When the pCO_2 = pCa_e, pore clogging will occur. Letters A to G represent aqueous compositions chosen for the present experiments. Circles [5] and diamonds [10] represent experimental conditions chosen by Duguid et al. for which no pore clogging was observed.

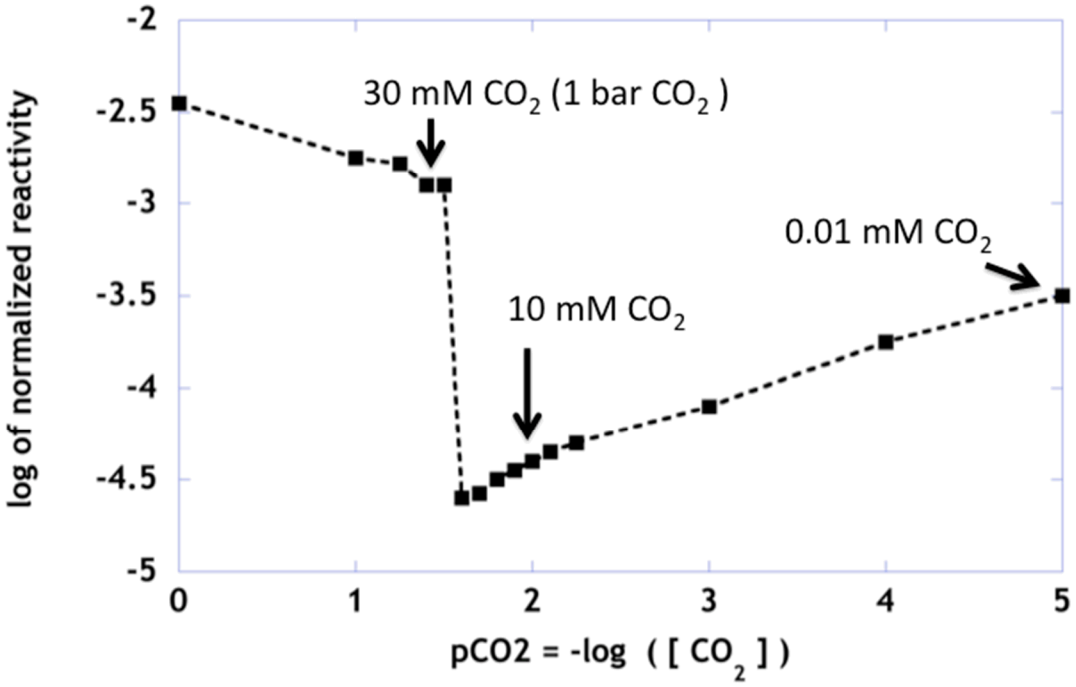

Figure 3. Plot of simulation data showing normalized reactivity versus pCO_2 (defined as $^{-}\log[CO_2]$). Reactivity is normalized by the self-diffusion coefficient of water. The plot shows a steep drop in reactivity in the region of $pCO_2 \approx 1.5$. From simulation alone, it is not clear whether this is an artifact or in fact a region where "pore-plugging" can be expected to occur.

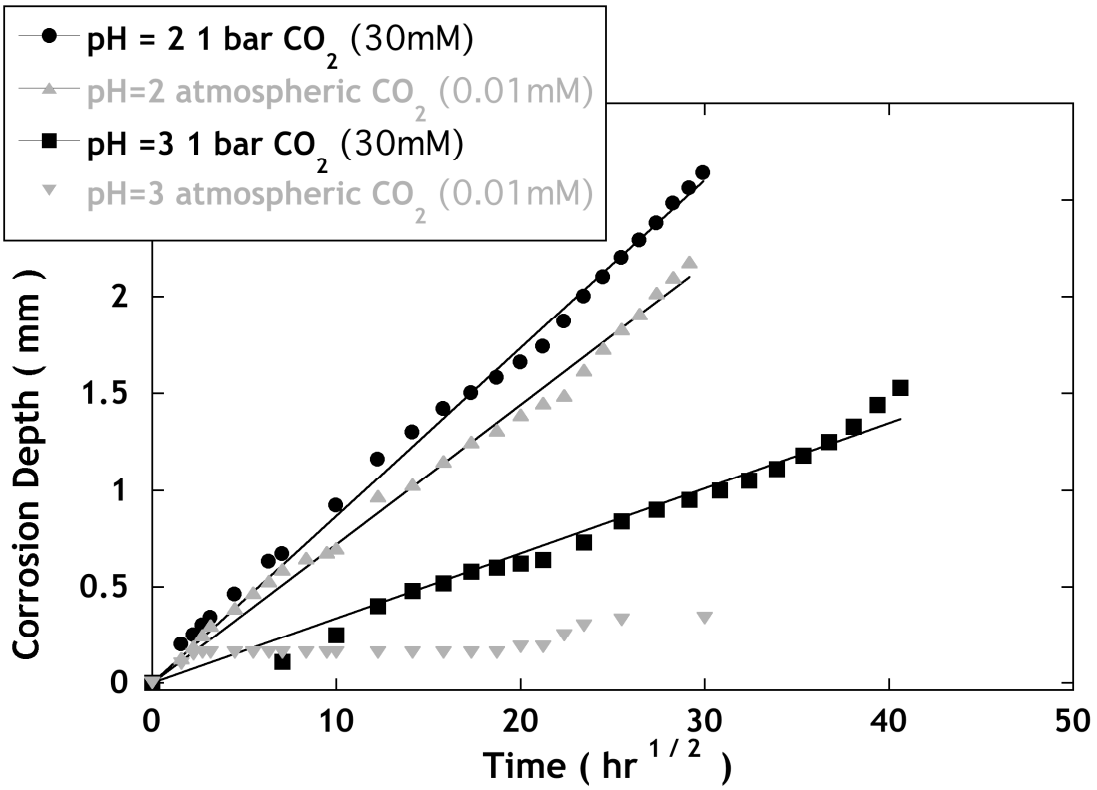

Figure 4. Plot of measured rates of both 1 bar CO_2 (30 mM CO_2) and "No CO_2" (0.01 mM , i.e. CO_2 content of solution in contact with atmospheric concentration of CO_2). The data clearly show that the rate of attack is greater for 30 mM CO_2 than for the 0.01 mM case, esp. at pH 3. The pH 3, 0.01 mM CO_2 case also deviates considerably from square-root of time kinetics. The plateaus in rate are real stops in rate of attack and are not related to measurement resolution.

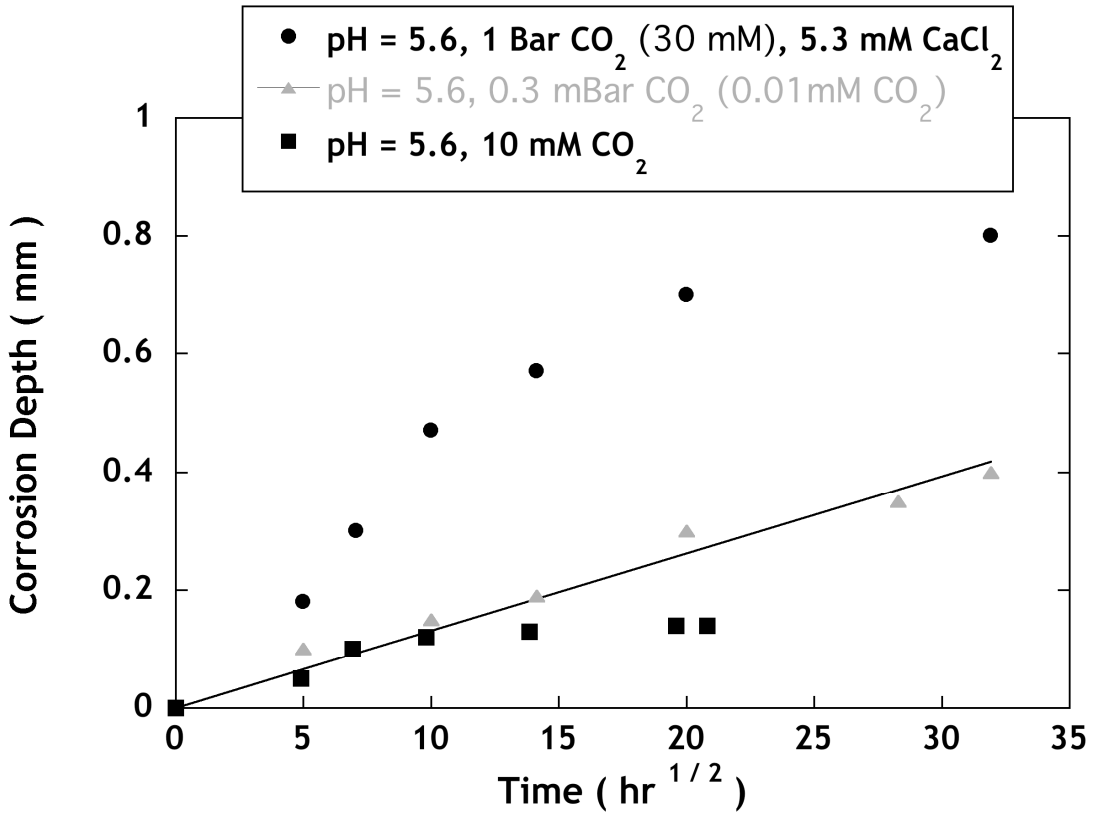

Figure 5. Flow-through benchtop experiments, all at pH 5.6, differing in dissolved CO_2 concentration. Only the 30 mM case (brine in equilibrium with atmoshperic CO_2) follows square root of time kinetics. The other two experiments deviate from the square-root of time dependence and, given the constant replenishment at the cement–acid interface, suggest that pore plugging is the cause.

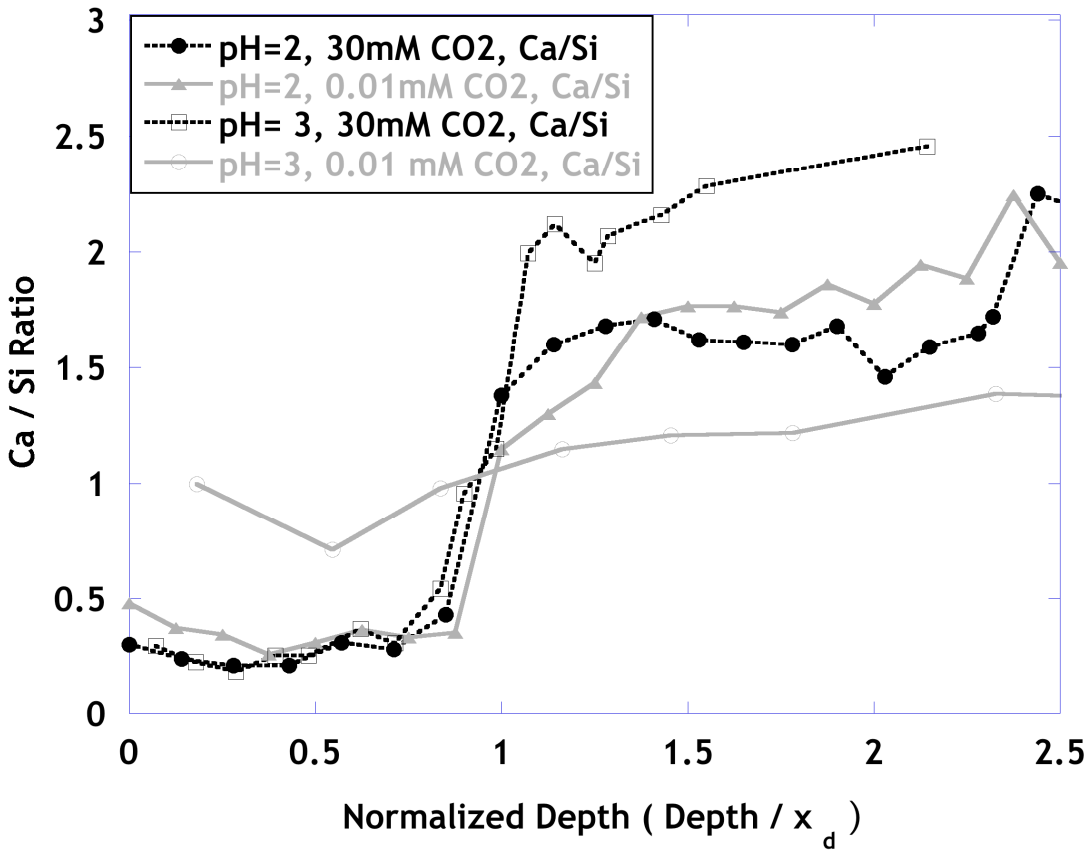

Figure 6. Calcium to silicon ratio of samples prepared at high (30 mM) and low (0.01 mM) CO_2 concentration. There is a low Ca/Si ratio in the calcium-leached gel region (0-1 on the x-axis) with a steep jump at the leading edge of the reaction. The jump marks the start of the calcium hydroxide-depleted region.

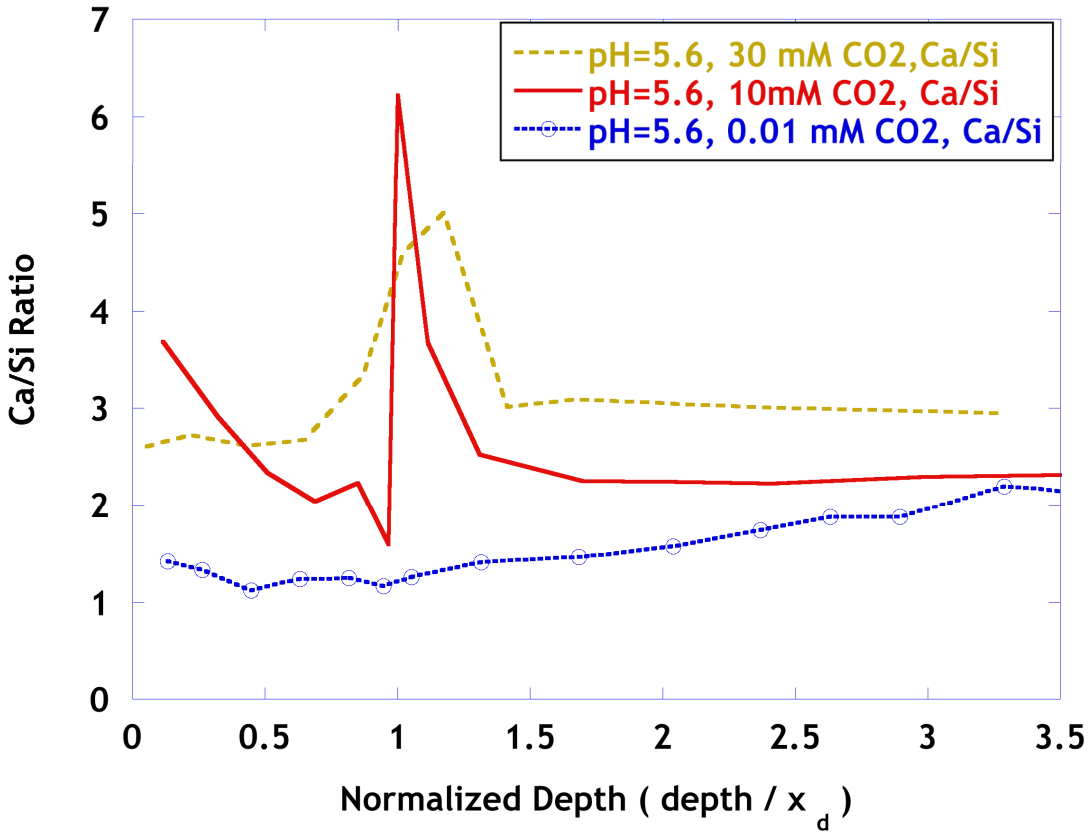

Figure 7. Ca/Si ratio for samples prepared to explore the pore-plugging behavior at pH 5.6. The compositional profiles indicate the presence of an enriched calcium layer in both the 30 mM and 10 mM CO_2 concentrations, which is not present in the brine containing only 0.01 mM CO_2.

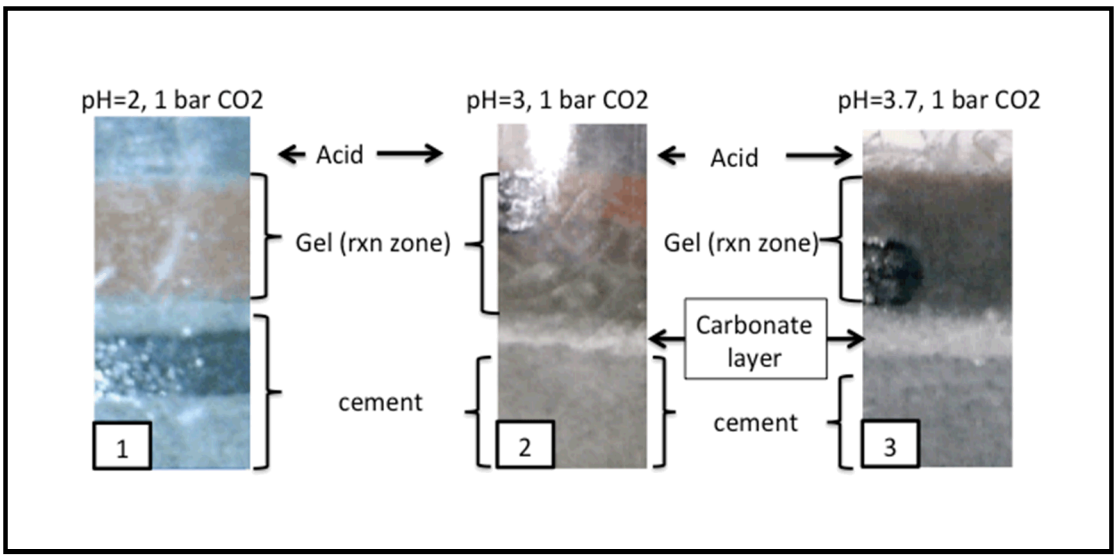

Figure 8. Comparison of carbonate layer thickness with increasing pH. As pH increases and the solubility of $CaCO_3$ decreases, the thickness of the carbonate increases significantly at equivalent depths of reaction.

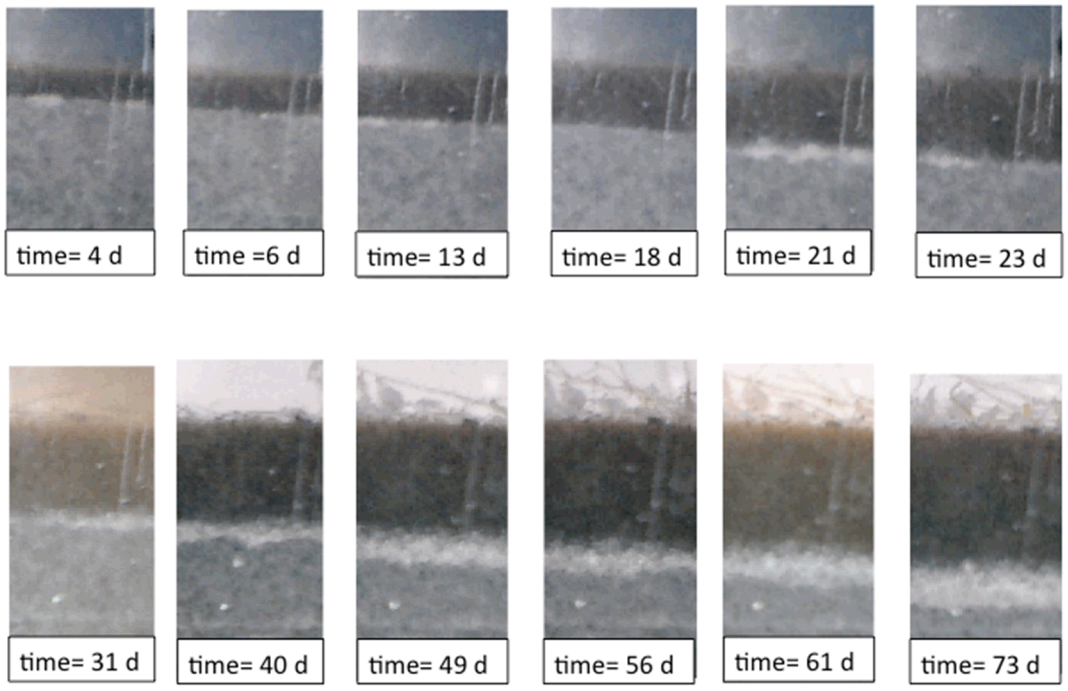

Figure 9. Evolution of $CaCO_3$ layer over time (in days). This sample was exposed to flow-through conditions (i.e., a continuous flow over the upper surface) and the brine was pH 3.7 saturated with CO_2 (30mM). The time series shows that while the carbonate increases overall in thickness, the layer "flickers," and at times appears to move laterally.

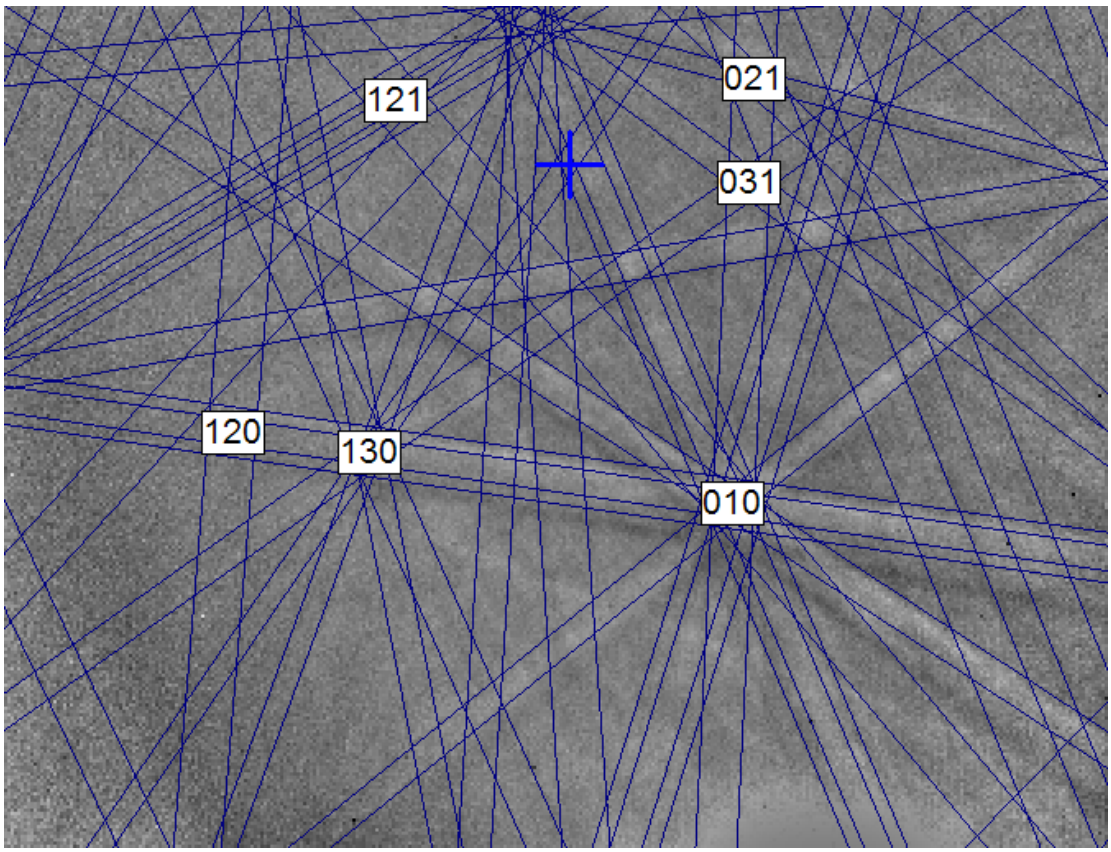

Figure 10. EBSD pattern in the area of high Ca/Si ratio (at the leading edge of the reaction front), has a strong match with calcite (mean angular deviation of 0.917).

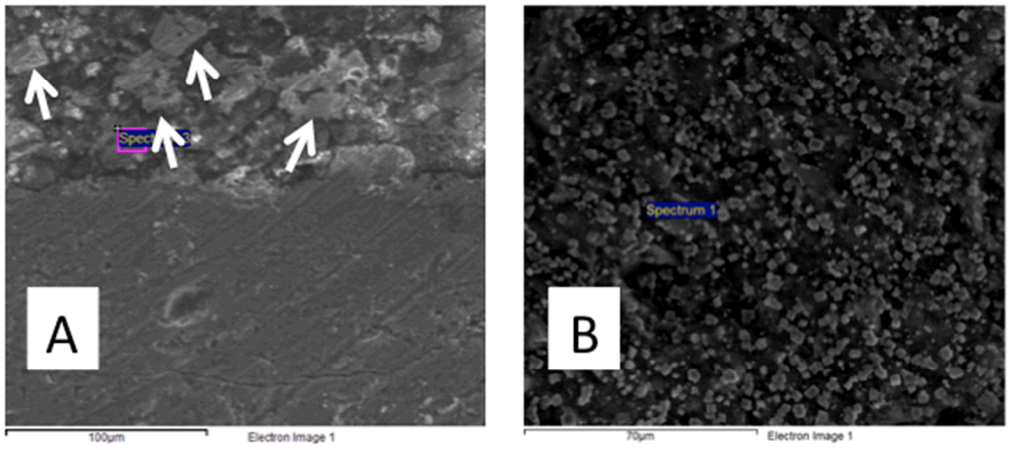

Figure 11. Comparison between gel microstructural features of pore-plugging experiments: (A) 10 mM CO_2 (scale bar =100 µm) and (B) 30 mM CO_2 (scale bar = 70 µm). Ca-rich features (brighter) for (A) range from 10 µm-30 µm (marked by white arrows), where as Ca-rich regions in (B) range from 1 to 5 µm.

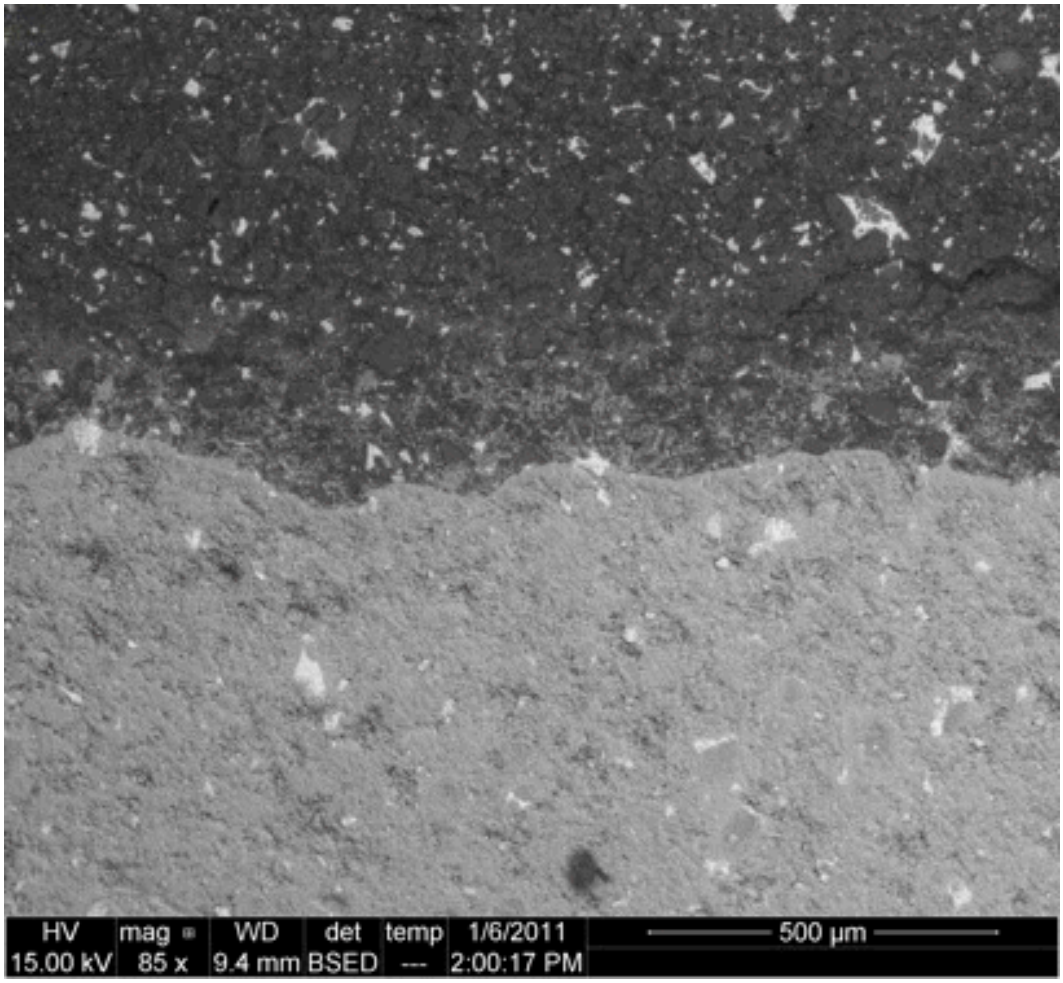

Figure 12. Back Scattered Electron image showing white flecks through the Ca-depleted silica gel (darker region in the upper half of the image). EDS identifies these flecks a being enriched in calcium relative to the surrounding matrix (see the following two Figures for EDS data).

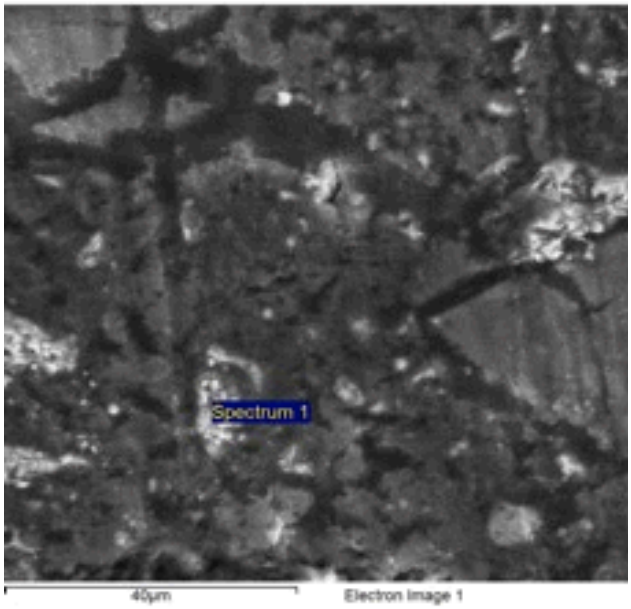

Element	Weight%	Atomic%
O K	53.64	71.52
Na K	0.88	0.82
Mg K	1.64	1.44
Al K	6.19	4.90
Si K	9.00	6.83
Cl K	0.80	0.48
K K	0.00	0.00
Ca K	22.49	11.97
Fe K	5.37	2.05

***Figure 13.** EDS summary of bright flecks in polished sample, showing that the region is enriched in Ca, with a Ca/Si ratio near 2.

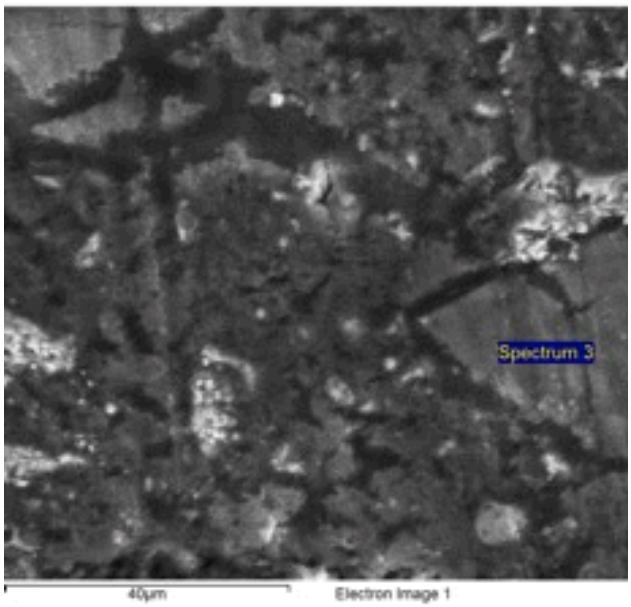

Element	Weight%	Atomic%
O K	50.74	65.37
Na K	2.42	2.17
Mg K	1.87	1.58
Al K	8.18	6.25
Si K	27.05	19.85
Cl K	2.23	1.30
K K	0.03	0.02
Ca K	4.88	2.51
Fe K	2.60	0.96

***Figure 14.** EDS summary showing that the darker features are depleted in Ca and richer in Si.

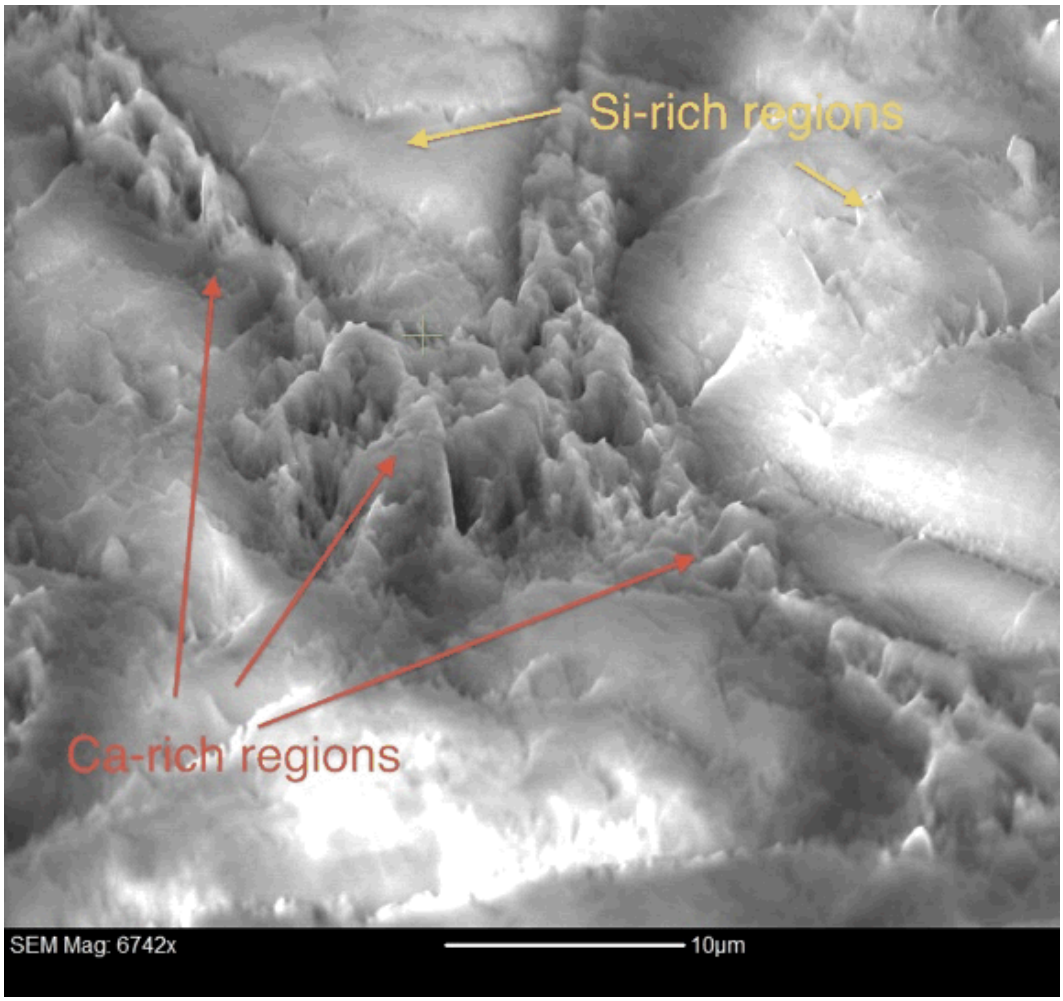

***Figure 15.** Close-up of the boundary between the calcium-rich and silicon-rich areas seen in the two previous figures. EBSD was performed on this spot and confirmed that the crystalline features seen in the Ca-rich regions are calcite.

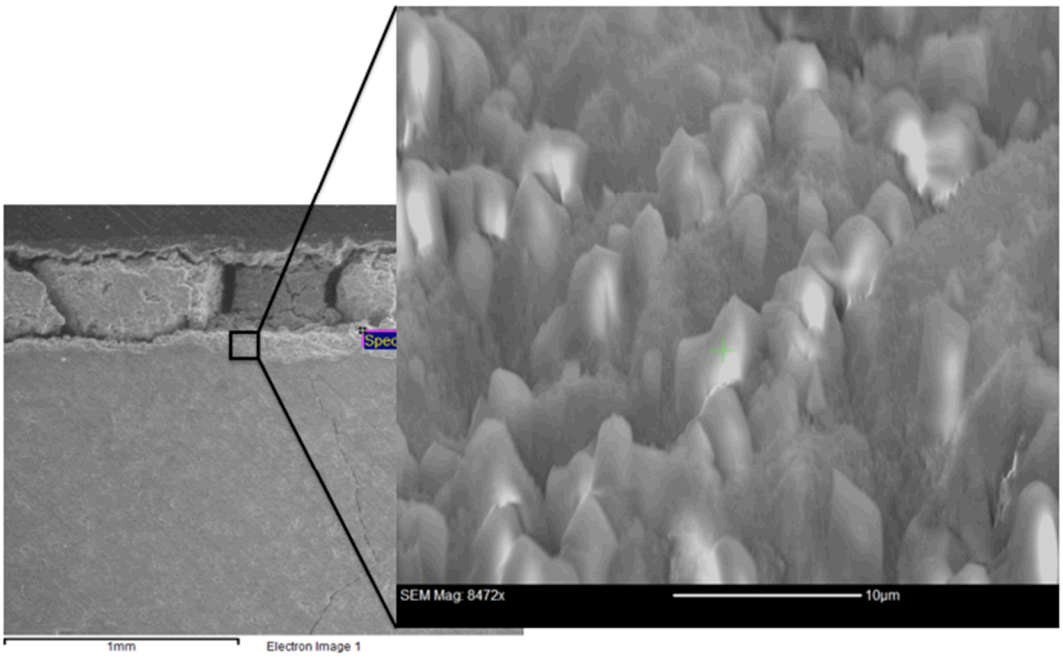

***Figure 16.** Enlargement of pore-blocking $CaCO_3$ layer in a sample exposed to a brine at pH 5.6, 30 mM CO_2. The EBSD pattern from this region is shown in Figure 9.

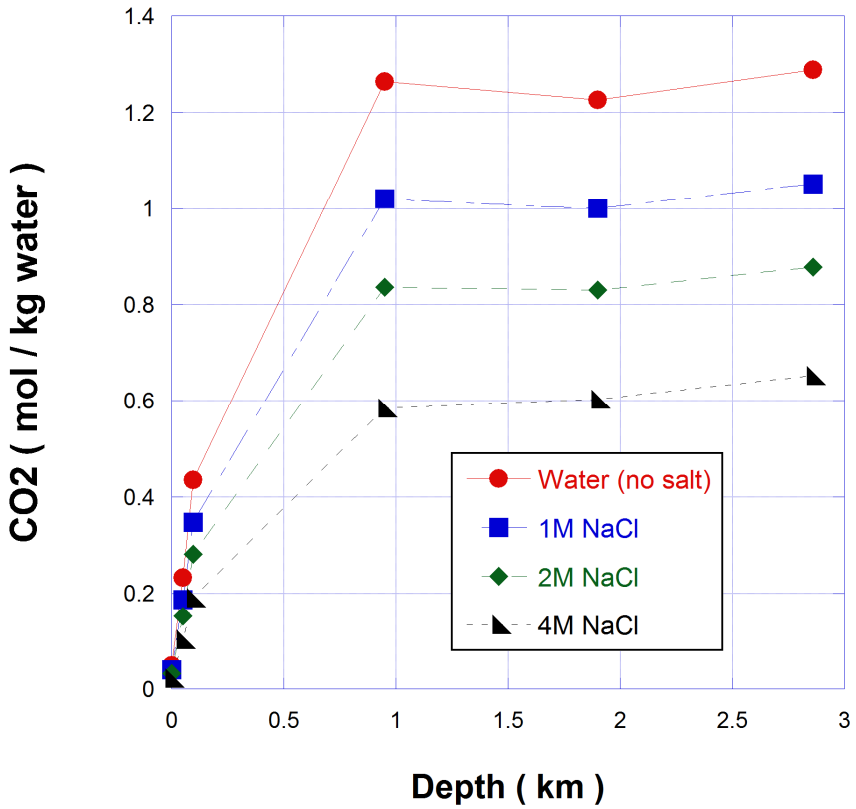

***Figure 17.** CO_2 concentration versus subsurface depth, calculated using CO_2 saturation data from Duan and Sun [29].